

Effect of Reynolds number and saturation level on gas diffusion in and out of a superhydrophobic surface

Hangjian Ling and Joseph Katz*

Department of Mechanical Engineering, Johns Hopkins University, Baltimore, Maryland 21218, USA

Matthew Fu and Marcus Hultmark

Department of Mechanical and Aerospace Engineering, Princeton University, Princeton, New Jersey 08544, USA

(Received 30 May 2017; published 26 December 2017)

This experimental study investigates the effects of ambient pressure and Reynolds number on the volume of a plastron in a superhydrophobic surface (SHS) due to compression and gas diffusion. The hierarchical SHS consists of nanotextured, $\sim 100\ \mu\text{m}$ wide spanwise grooves. Microscopic observations measure the time evolution of interface height and contact angle. The water tunnel tests are performed both without flow as well as in transitional and turbulent boundary layers at several Reynolds numbers. Particle image velocimetry is used for estimating the wall shear stress and calculating the momentum thickness for the SHSs under Cassie-Baxter (CB) and Wenzel states as well as a smooth wall at the same conditions. Holographic microscopy is used for determining the wall shear stress directly for one of the CB cases. The mass diffusion rate is calculated from changes to the plastron volume when the liquid is under- or supersaturated. For stationary water, the mass diffusion is slow. With increasing pressure, the interface is initially pinned and then migrates into the groove with high advancing contact angle. Upon subsequent decrease in pressure, the interface migrates upward at a shallow angle and, after being pinned to the tip corner, becomes convex. With flow and exposure to undersaturated liquid, the diffusion-induced wetting also involves pinned and downward migration states, followed by shrinkage of the plastron until it decreases below the resolution limit. The corresponding changes to the velocity profile indicate a transition from slight drag reduction to significant drag increase. In supersaturated water starting at a Wenzel state, a bubble grows from one of the bottom corners until it reaches the other side of the groove. Subsequently, dewetting involves upward migration of the interface, pinning to the tip corners, and formation of a convex interface. The diffusion rate increases with the level of under- or supersaturation and with the Reynolds number. A power law relation, $\text{Sh}_{\theta 0} = 0.47\text{Re}_{\theta 0}^{0.77}$, is obtained for the turbulent flow regime using the smooth wall momentum thickness for calculating the Sherwood ($\text{Sh}_{\theta 0}$) and Reynolds ($\text{Re}_{\theta 0}$) numbers. This relation agrees with published diffusion rates for smooth wall turbulent boundary layers. However, the mass diffusion rate is lower than this prediction in the transitional boundary layer. When $\text{Sh}_{\theta 0}$ is plotted against the friction Reynolds number ($\text{Re}_{\tau 0}$) instead, both the transitional and turbulent boundary layer results collapse onto a single power law, $\text{Sh}_{\theta 0} = 0.34\text{Re}_{\tau 0}^{0.913}$. This trend suggests that turbulent diffusion and wall friction are correlated. The relation between Sherwood number and momentum thickness Reynolds number persists if length scales of the Wenzel state are used instead of those of the smooth wall. However, trends with the friction Reynolds number change slightly.

DOI: [10.1103/PhysRevFluids.2.124005](https://doi.org/10.1103/PhysRevFluids.2.124005)

*katz@jhu.edu

I. INTRODUCTION

Two states are possible when a micro- or nanotextured superhydrophobic surface (SHS) comes into contact with liquid, the Cassie-Baxter (CB) state, where gas or plastron is trapped between the textures, and the Wenzel state, where the trapped gas is replaced by liquid [1]. The CB state is desirable due to its potential for self-cleaning, drag reduction, and ice or biofouling resistance [2–6]. Transition to a Wenzel state and resulting loss of superhydrophobicity can be promoted by an increase of hydrostatic pressure, diffusion of gas, entrainment by turbulent flow, and other mechanisms [7–12]. Thus, understanding the effect of pressure and flow on the state of the surface is essential for the design of SHSs. Two criteria are generally used to predict the stability of the CB state. The first is based on thermodynamic free energy balance [13]. The second is derived from the balance between surface tension γ and the pressure difference across the plastron-liquid interface, $\Delta p = p_w - p_p$, where p_w and p_p are the liquid and plastron pressures, respectively. To maintain a CB state on a groove with width w , the maximum pressure difference is $\Delta p_{\max} = -2\gamma \cos\theta_{adv}/w$, where θ_{adv} is the local advancing contact angle [2]. For an SHS with a single-level topography, θ_{adv} typically falls within $110^\circ \leq \theta_{adv} \leq 120^\circ$ [14–18]. Hierarchical textures involving nanoplastron on the side walls of the microtextures have been proposed as a means to achieve $\theta_{adv} > 120^\circ$ [19,20]. The magnitude of Δp_{\max} ranges from $O(10^2)$ Pa for microtextures [15] to $O(10^5)$ Pa for nanotextures [18].

Even when the above criteria are satisfied, since the solubility of dissolved gas increases with pressure, gas diffusion out of the plastron might also cause a wetting transition. Change of the SHS state due to gas diffusion has been determined by illuminating surfaces at the total internal reflection angle and observing changes to the intensity of reflection from the surface [21–27]. This approach has been used in stationary liquid [21–23], laminar microchannel flows [24,25], laminar boundary layers [26], and for jets injected parallel to a surface [27]. Confocal microscopy [22,28–30] and direct imaging [31] have also been used to measure the height of the interface within the textures to calculate the diffusion rate in stationary liquid [22,28,31] and laminar microchannel flows [29]. Numerical simulations [32,33] and theoretical predictions [28,31] of the interface shape and lifetime of the CB state in stationary liquid have been performed by specifying the mass transfer coefficient of gas. Simulations for a laminar boundary layer assuming a flat, shear-free interface have also been implemented [34]. Diffusion rate estimates for a turbulent boundary layer has been based on a theoretical integral analysis involving assumed velocity profiles as well as eddy viscosity and mass diffusivity [35]. To the best of our knowledge, the mass diffusion rate has never been measured for a turbulent boundary layer.

The mass flux from plastron to liquid per unit area, J , can be approximated using Fick's law [36] as $J = D(c_i - c_\infty)/\delta_c$, where D is the diffusion coefficient, c_i and c_∞ are the gas concentrations in the liquid at the interface and in the bulk, respectively, and δ_c is the gas diffusion length scale. According to Henry's law, $c_i = p_g/k_H$, where p_g is partial pressure of gas in the plastron, and k_H is the Henry's law constant. For convenience, we also define $p_\infty = k_H c_\infty$ to represent the saturation pressure corresponding to c_∞ . Considering the plastron contains both gas and water vapor, $p_p = p_g + p_v$, where p_v is the water vapor pressure. For a two-dimensional (2D) plastron within a groove, $p_p = p_w + 2\gamma \cos\theta_{CL}/w$, where θ_{CL} is the local contact angle. Therefore,

$$J = D(p_w + 2\gamma \cos\theta_{CL}/w - p_v - p_\infty)/(k_H \delta_c). \quad (1)$$

The CB state could be maintained when $J \leq 0$ [24–26,31], but wetting transition is expected to occur as p_w increases to a level that $J > 0$. For flow with a characteristic length scale of δ , e.g., boundary layer or channel height, J is typically nondimensionalized into the Sherwood number, $Sh_\delta = \delta/\delta_c$ [37]. There are several reported relationships between Sh_δ and the Reynolds number, $Re_\delta = U\delta/\nu$, where U and ν are the characteristic velocity and liquid kinematic viscosity, respectively. In a laminar channel flow at $0 < Re_\delta < 20$ and at a fixed streamwise location, Xiang *et al.* [29] show that $Sh_\delta \propto Re_\delta^{1/3}$. For a laminar boundary layer, simulations by Barth *et al.* [34] show that Sh_δ is independent of Re_δ . The classical relation for mass transfer for a turbulent boundary

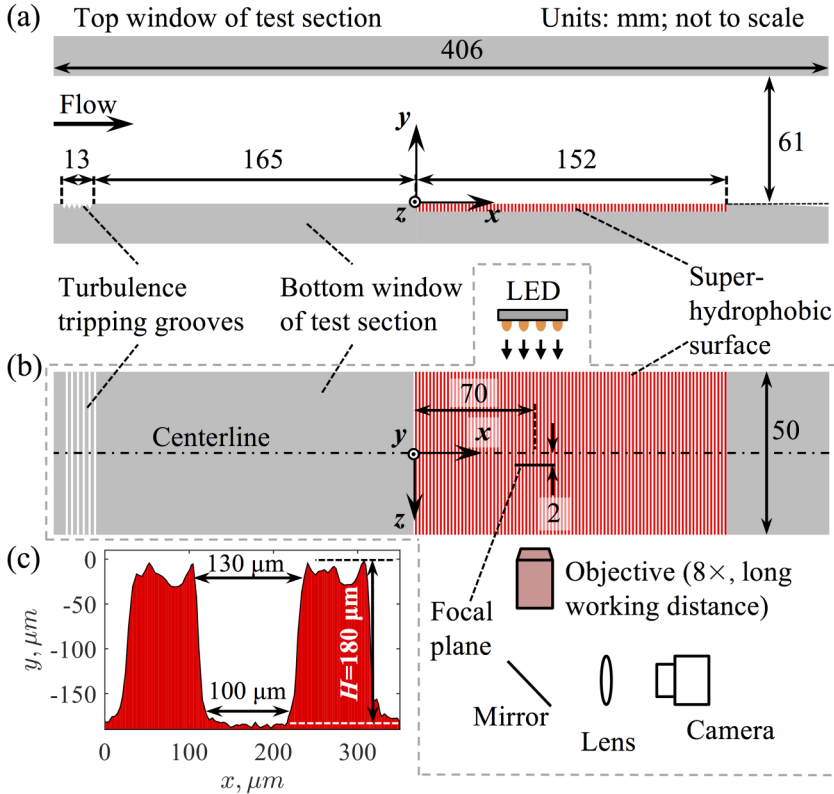


FIG. 1. The experimental setup showing (a) the side and (b) top views of the test section of the water tunnel and the optical setup for imaging the plastron and (c) a sample profile of a single groove of the SHS.

layer over a solid flat plate [37,38] is $Sh_\delta \propto Re_\delta^{0.75}$, assuming that $\delta/x \propto (Ux/\nu)^{-0.2}$, where x is the streamwise distance. Barth *et al.* [35] propose that the same relation applies to a slip boundary layer. However, this relation has yet to be proven either numerically or experimentally.

In this study, we examine experimentally the behavior of the gas-liquid interface on an SHS resulting from changes to the ambient pressure without and with flow, the latter covering transitional and turbulent boundary layers. The direct observations enable us to measure the local contact angle and interface height during wetting and dewetting transitions, as well as calculate the mass diffusion rate out of and into the plastron. The data are used for determining the relation between Sh_δ and Re_δ . The experimental procedures are described in Sec. II, followed by the results and analysis in Sec. III.

II. EXPERIMENTAL PROCEDURES

The experiments are performed in a small, high-speed water tunnel described in Refs. [39,40], the same facility used for recent velocity measurements in the inner part of turbulent boundary layer over SHSs [12]. The flow is driven by two 15 HP (maximum) centrifugal pumps located 5 m below the test section and passes through a settling tank, a settling chamber containing honeycombs and screens, and a 9:1 contraction before entering the test section. The 406-mm-long, 61-mm-high, and 50-mm-wide transparent test section is illustrated in Figs. 1(a) and 1(b). At the entrance of the test section, the bottom wall contains a series of machined spanwise tripping grooves aimed at forcing early boundary layer transition to turbulence, as verified by the velocity measurements. The 152-mm-long and 50-mm-wide SHS is flush mounted on the bottom wall and locates 165 mm

downstream of the tripping grooves. In the selected coordinate system, x , y , and z denote the streamwise, wall-normal, and spanwise directions, respectively, with $x = 0$ coinciding with the leading edge of the SHS, $y = 0$ with the tip of grooves, and $z = 0$ the centerline of test section. The corresponding instantaneous velocity components are (u, v, w) , and ensemble-averaged values are denoted as (U, V, W) .

Figure 1(c) shows a sample profile of one groove of SHS obtained using confocal laser scanning microscopy. The periodicity of spanwise groove is $200 \mu\text{m}$, its height is $H = 210 \pm 35 \mu\text{m}$, varying in the spanwise and axial directions ($180 \mu\text{m}$ for the sample shown), and its width, w , decreases from $130 \mu\text{m}$ at the top to $100 \mu\text{m}$ at the bottom. The SHS is fabricated on a 2024 aluminum substrate using the following procedures: First, the spanwise grooves are fabricated by a slitting saw. Second, following the procedures described in Ref. [41], nanotextures are generated by boiling the sample in deionized water for approximately 15 min. A typical SEM image of the nanotextures generated using the same procedure can be found in Ref. [41]. Third, the hydrophobic functionalization is performed by immersing the sample overnight in an ethanol-based solution containing 1% (by weight) of Masurf FS100 (Pilot Chemical Co.), a phosphate ester with mixed length of fluorinated alkyl chains [41].

The optical setup to measure the shape of the interface is shown in Fig. 1(b). The surface is illuminated in the spanwise direction by a collimated LED light, and images are recorded by a high-speed camera (PCO.Dimax HD). An $8\times$, infinity corrected, long working distance microscope objective is inserted before the camera to magnify the image and achieve a resolution of $1.3 \mu\text{m}/\text{pixel}$. The center of the in-focus plane is located at $x = 70 \text{ mm}$ and $z = 2 \text{ mm}$. The image acquisition rates vary, with the highest level, 40,000 frames per second (fps) for an image size of $1.2 \times 0.3 \text{ mm}$, being used for examining the flow-induced interface vibrations. For characterizing the relatively slow diffusion process, the images are recorded at 10 fps.

Although the detailed velocity distributions are not of primary interest in a study focusing on mass diffusion, we have measured the characteristic length scales of the boundary layer for the purpose of developing empirical relations between Sh_δ and Re_δ . In the current study, the mean tunnel speed (flow rate divided by the tunnel cross section), U_m , varies between 0.65 to 2.2 m/s, as measured using an electromagnetic flow meter. The velocity profile in the boundary layer in the abovementioned imaging region is characterized by 2D particle image velocimetry (PIV) at a resolution that covers the entire boundary layer, and dual-view digital holographic microscopy (DHM) at a magnification that fully resolves the flow structure in the inner part of the boundary layer [12]. In the PIV measurements, the instantaneous velocity in the x - y plane is calculated using an in-house developed code [42] to calculate the spatial cross-correlations using a rectangular interrogation window of size $346 \mu\text{m} \times 86 \mu\text{m}$ ($x \times y$). With 50% overlap between windows, the vector spacing is $173 \mu\text{m} \times 43 \mu\text{m}$. The field of view is $36 \times 24 \text{ mm}^2$ ($x \times y$). For DHM measurements, the instantaneous velocity is calculated using particle-tracking velocimetry, followed by first-order Taylor series expansion and singular value decomposition [12,43,44] to interpolate the data onto three-dimensional regular grids with spacing of $120 \mu\text{m} \times 10 \mu\text{m} \times 240 \mu\text{m}$ ($x \times y \times z$). The field of view is $4.4 \times 2.4 \times 3.2 \text{ mm}^3$ ($x \times y \times z$). For both PIV and DHM, the mean flow quantities are obtained by local ensemble averaging over more than 500 realizations, followed by spatial averaging in the x direction for the PIV data over 205 lines, and in the x and z directions for the DHM data over 468 profiles.

Baseline PIV measurements for a smooth wall have been performed at the same location by replacing the SHS with a solid surface. The data are used for estimating the wall friction by a fit to the log layer in the turbulent Reynolds number range and by a fit to the mean velocity profile near the wall for the transitional case, taking advantage of the relatively larger length scales. The log-law fit for the smooth wall (only) is performed using a von Karman constant $\kappa = 0.41$ over the vertical span where the magnitude of $y dU/dy$ is almost constant, namely, $30 < y/\delta_v < 120$. The baseline mean flow quantities for four different U_m are listed in Table I, including U_0 the freestream velocity at the top of the boundary layer, δ the boundary layer thickness based on 99% of U_0 , Θ the momentum thickness obtained by integrating the velocity profile, τ_w the wall shear stress, $\delta_v = \nu(\rho_w/\tau_w)^{0.5}$ the

TABLE I. Boundary layer parameters for a smooth wall as well as the SHS in Cassie-Baxter and Wenzel states for the same location in the water tunnel.

Surfaces	U_m , m/s	U_0 , m/s	δ , mm	Θ , mm	τ_w , Pa	δ_v , μm	Re_Θ	Re_τ
Smooth wall (2D PIV)	0.65	0.68	7.15	0.76	0.78	35.7	518	200
	1.05	1.10	7.84	0.82	2.70	19.2	900	408
	1.58	1.65	8.44	0.87	5.48	13.5	1429	625
	2.11	2.21	8.70	0.94	8.84	10.6	2088	820
SHS _{CB} (DHM)	2.13	–	–	–	8.46	11.8	–	–
SHS _{CB} (2D PIV)	2.13	2.23	9.57	0.93	8.93	–	2080	–
	0.66	0.69	6.13	0.63	–	–	433	–
SHS _W (2D PIV)	1.07	1.11	7.17	0.78	2.90	18.5	862	387
	1.61	1.67	7.60	0.84	7.92	11.2	1406	678
	2.11	2.20	7.77	0.89	14.4	8.3	1968	936

viscous length scale, where ρ_w is the liquid density, as well as $\text{Re}_\Theta = U_0\Theta/\nu$, and $\text{Re}_\tau = \delta/\delta_v$. The range of Re_Θ , 518–2088, covers both transitional and turbulent regimes, as confirmed later in this paper. Since U_0 corresponds to a displacement of ~ 40 pixels, using a conservative estimate for the uncertainty in particle displacement of 0.5 pixel, the uncertainty in instantaneous velocity is about 1.25% of U_0 . By averaging more than 500 realizations, the uncertainty in mean velocity associated with random errors is in the order of 0.1% of U_0 . The resulting uncertainty in Θ is about 1%.

Figure 2(a) presents the baseline wall friction coefficient, $f_0 = \tau_{w0}/(0.5\rho_w U_0^2)$, as a function of $\text{Re}_{\Theta 0}$ based on the quantities listed in Table I. Here and below, a subscript 0 denotes quantities measured for the baseline flow at the same U_m . The measured magnitudes and trends agree well with the DNS data of Wu and Moin [45], which is also plotted. For $\text{Re}_{\Theta 0} \geq 900$, the values of f_0 fall on the classical power law $f_0 \sim \text{Re}_{\Theta 0}^{-0.25}$ [46] confirming that the boundary layer is turbulent. For the lowest Reynolds number, $\text{Re}_{\Theta 0} = 518$, the magnitude of f_0 is significantly lower than the turbulent power law prediction and higher than trends of a laminar boundary layer, indicating, consistent with the DNS results, that the boundary layer is transitional. Figure 2(b) shows the smooth wall mean velocity profiles for the current four Reynolds numbers along with one obtained in the same facility (very similar tripping and location) and discussed in Ling *et al.* [12]. The latter has been measured using holographic microscopy, which resolves the viscous sublayer and allows direct measurement of wall shear stress from the velocity gradients in the viscous sublayer. The values are scaled with

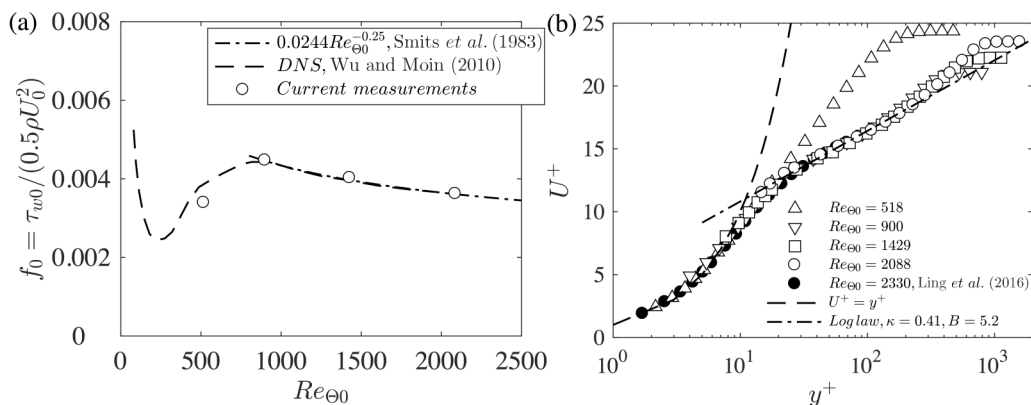


FIG. 2. (a) Baseline wall friction coefficient for the smooth wall as a function of $\text{Re}_{\Theta 0}$ compared to the DNS results of Ref. [45] and (b) mean velocity profiles of the smooth walls for the current four Reynolds numbers obtained by 2D PIV along with sample data from Ref. [12] obtained using digital holographic microscopy.

inner variables, $U^+(y^+)$, where $y^+ = y/\delta_v$, $U^+ = U/u_\tau$, and $u_\tau = (\tau_w/\rho_w)^{0.5}$. As expected, all the turbulent velocity profiles ($\text{Re}_{\Theta} > 800$) collapse in the log and buffer layer. In the outer layer, both U^+ and δ^+ increase with the Reynolds number [47]. Conversely, at $\text{Re}_{\Theta} = 518$, the near wall profile ($y^+ < 10$) agrees with that of a laminar boundary layer but falls between the laminar and log law profiles at higher elevations. Profiles of the Reynolds normal and shear stresses in turbulent region are also consistent with expected trends, as shown in Ling *et al.* [12].

For the same surface and streamwise distance, one should expect a decrease in boundary layer thickness with increasing mean tunnel speed ($\Theta \sim U_0^{-0.14}$ [47]). However, Table I shows that in the current measurements, the smooth wall boundary layer and momentum thicknesses increase with increasing tunnel speed. The probable cause for this trend involves the effect of the tripping grooves at the entrance to the test section. With increasing tunnel speed, the roughness height of the tripping grooves normalized by the local viscous wall unit increases. Hence, the impact of the grooves on the boundary layer thickness is likely to increase with freestream velocity. Consequently, one may question whether the structure of the present turbulent boundary layers is consistent with naturally developing ones. However, the present measurements are performed 29 – 33 δ downstream of the groove, and the following series of criteria can be used for demonstrating that the structure of the current turbulent boundary layers is consistent with that of natural ones: (i) As demonstrated in Fig. 2(b) and in Ling *et al.* [12] for the same setup, the mean velocity profiles in the buffer and log layers collapse to the classic profile. (ii) There is excellent agreement between the directly measured wall friction and that determined from the log layer profile. (iii) There is very good agreement between the presently measured $f_0 - \text{Re}_{\Theta}$ relationship with published DNS results in [45]. (iv) Ling *et al.* [12] show that profiles of the Reynolds normal and shear stresses follow the expected trends with Reynolds number.

The DHM measurement has been used for determining the τ_w of the SHS in the CB state at $U_m = 2.13$ m/s. Following the procedures in Ling *et al.* [12], in this case, τ_w is calculated by summing the Reynolds shear stress at the top of the grooves and the viscous stress ($\rho_w v dU/dy$), where the velocity gradient is determined by a linear fit to the mean velocity profile at $y < 60$ μm . Results are denoted as SHS_{CB}, and summarized in Table I. It shows a 4% reduction of wall friction. PIV has been utilized for measuring the mean velocity profiles over the SHS in the Wenzel state, after wetting the SHS at high pressure. The results are denoted as SHS_W in Table I. In these cases, τ_w are estimated from a logarithmic fit to mean velocity profile at $30 < y/\delta_v < 120$, similar to the procedures used for the baseline cases. This estimate may differ from the true wall friction due to the short distance ($x = 8\delta$) from the front of the grooved surface [12,48]. For an SHS where roughness effect is dominant, Ling *et al.* [12] show that at $x = 4\delta$, τ_w estimated from a log law fit is 12% higher than the directly measured value. For spanwise grooves with $H/\delta_v \sim 40$, i.e., similar to the present highest Re_{Θ} case, direct numerical simulations (DNSs) by Lee [44] show that the equilibrium log layer is established at $x > 7\delta$. Therefore, the log fit based estimate of the τ_w is reasonable for the purpose of evaluating the associated Reynolds numbers. As is evident, for case $U_m = 2.11$ m/s, τ_w at the Wenzel state is 70% higher than that of the CB state for the same surface, speed, and location. The 2D PIV measurements have also been performed for the CB state at $U_m = 2.13$ m/s for calculating the boundary layer length scales and the corresponding Reynolds numbers. In this case, the smooth wall and CB results do not differ significantly and are shown in Table I.

According to the integral momentum equation, for two surfaces at same mean tunnel speed and same streamwise distance, the momentum thickness should increase with wall friction. However, as demonstrated and discussed in Ling *et al.* [12], the present SHS is too short for reaching equilibrium conditions. Consequently, the outer layer scales, including the boundary layer thickness, are not likely to fully adjust to the change in surface conditions. Hence, for the same velocity, one should expect a higher momentum thickness over the SHS in the Wenzel state than that for smooth wall, but not to the level reflecting the change in wall friction. Yet Table I shows that the momentum thickness for SHS in Wenzel state is actually 5% lower than that of the smooth wall. This small difference

might be caused by a slight change in the flow at the entrance to the test section that occurs as the surfaces are replaced. These differences do not affect the scaling laws introduced in Sec. III, since they are calculated using the momentum thickness for the same surface, and reconfirmed by repeating the analysis for the other.

The pressure in the test section is controlled by connecting a compressor and a vacuum pump to an air-water interface located in a chamber well above the test section [39]. The value of p_w is monitored by a pressure transducer connected to a tap located at the bottom wall of the test section, 140 mm upstream of the SHS. In the current study, the absolute value of p_w varies from 0.9 to 1.9 atm. The temperature of bulk liquid is maintained at 23 ± 1 °C, corresponding to $p_v = 0.03$ atm. The concentration of dissolved air in water is inferred from measurement of dissolved oxygen using an optical sensor (FirestingO₂, Pyro Science). The concentrations of O₂ and N₂ in water at atmospheric pressure and temperature of 23 °C, are 8.6 and 14.1 mg/l, respectively, and the ratio between these values is maintained as long as the nearby air composition does not change [49]. The sensor is calibrated and the concentration measurements are performed prior to each experiment. The associated uncertainty is ± 0.1 mg/l, as specified by the manufacturer. To establish elevated dissolved gas content, air bubbles are injected into the water through a series of 100 μm holes located at the bottom wall of the test section while running the tunnel at $U_m = 5$ m/s and $p_w \sim 0.9$ atm for about 4 hr prior to each experiment. It should be noted that p_w is the lowest pressure in the facility, and the corresponding pressure in the 1000 l storage tank upstream of the test section is well above the atmospheric pressure (~ 1.2 atm). Consequently, all the present tests are performed at a concentration of 9.5 mg/l of O₂, corresponding to $p_\infty = 1.10$ atm using the Henry constant for oxygen (11.6 atm m³/g). The total dissolved air concentration is $c_\infty = 25.1$ mg/l. Since the magnitude of $p_w - p_\infty - p_v$ under the present conditions is much larger than that of $2\gamma\cos\theta_{CL}/w$, the effect of surface tension on J is ignored in the following analysis. Accounting for the vapor pressure, Eq. (1) indicates that one should expect $J > 0$ when $p_w > 1.13$ atm, and $J < 0$ when $p_w < 1.13$ atm.

III. RESULTS AND DISCUSSIONS

Figure 3 compares mean velocity profiles scaled with inner variables for very similar freestream velocities. Here, and in the following discussion, the subscripts CB and W denote quantities measured for SHS in CB and Wenzel states, respectively. Included are baselines cases at $Re_{\theta_0} = 2088$, SHS_W

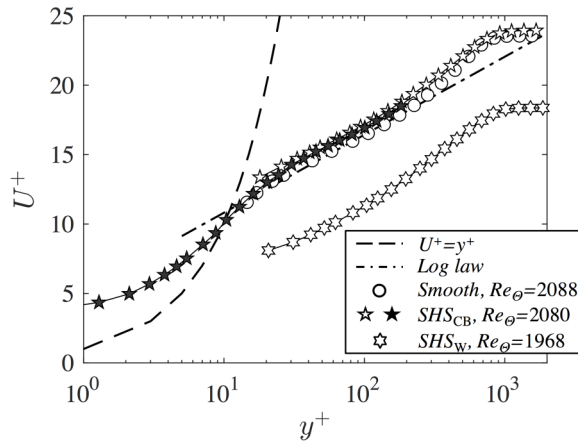


FIG. 3. Mean velocity profiles for the smooth wall at $U_m = 2.11$ m/s ($Re_{\theta_0} = 2088$), as well as at $U_m = 2.13$ m/s for the SHS in Cassie-Baxter ($Re_{\theta_{CB}} = 2080$) and Wenzel ($Re_{\theta_W} = 1968$) states. The hollow symbols show data obtained using 2D PIV, and the full symbols show the DHM results.

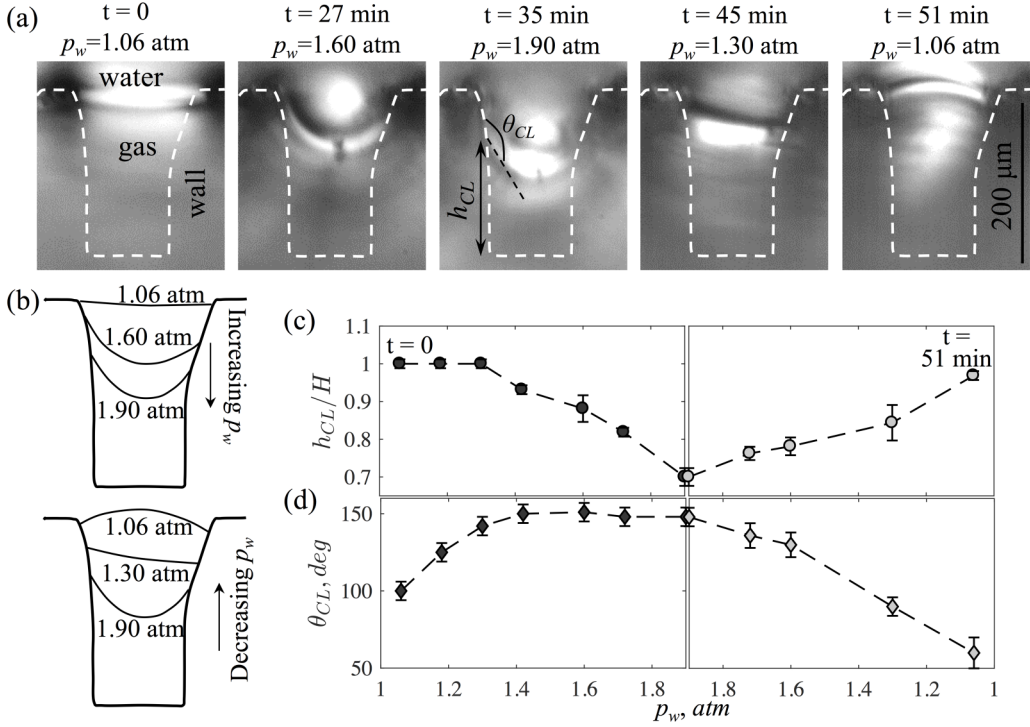


FIG. 4. The response of a submerged plastron to an increase and subsequent decrease in ambient pressure with no flow: (a) selected images for the specified timing and p_w ; (b) measured schematics of the interface shape; (c) corresponding interface height at the contact line averaged of the two sides; and (d) the local contact angle (averaged).

at $Re_{\Theta W} = 1968$, as well as two SHS_{CB} results measured at $U_m = 2.13$ m/s. The first is obtained using DHM and focuses on the inner part of the boundary layer, and the second is based on the 2D PIV data, for which $Re_{\Theta CB} = 2080$. Since the profiles collapse into each other in overlapping elevations, we refer to both using the same Reynolds numbers. The SHS_{CB} profile is shifted upward slightly in the log region and significantly in the viscous sublayer compared to baseline case, consistent with the 4% reduction in wall friction. Such an upward shift has been observed for simulated or measured drag reduction cases [12,50–52]. In contrast, the SHS_W profile is shifted downward significantly, consistent with trends of rough wall boundary layers [53]. The difference between the SHS_{CB} and SHS_W results demonstrates the effect of the plastron since the surface and freestream velocity are identical.

As a reference, the effect of pressure on the plastron behavior is examined initially *without flow*, as summarized in Figs. 4(a)–4(d). The experiment consists of gradually increasing p_w from 1.0 to 1.9 atm and then decreasing p_w back to 1.0 atm. For each indicated data point, the interface shape is measured after keeping the pressure at the indicated level for more than 10 s. The entire cycle lasts 51 min. Figure 4(a) provides a series sample characteristic images of the plastron, and Fig. 4(b) shows the corresponding plastron shape measured directly from the images. In most cases, the interface is a bright thick line connecting the two sidewalls of the groove. The center of this line is treated as the interface location, and the upper and lower boundaries of this line define the uncertainty in the measurement. The experiment involves measurements of the time evolution of θ_{CL} (averaged value of two sides) and the averaged interface height at the contact line, h_{CL} . Both are illustrated in one of the images. Since the molecular diffusion coefficient is very small ($\sim 10^{-9}$ m²/s) in stationary liquid, one should expect little mass diffusion in and out of the plastron during this

experiment. This postulate has been confirmed by using the plastron shape [Fig. 4(b)] for calculating and comparing the volume of gas in the plastron at the beginning and at the end of the experiment (after 51 min), keeping in mind that the liquid is undersaturated most of the time. The volumes differ by less than 5%, which is barely above the uncertainty level. Hence, we neglect the effect of mass diffusion in the following discussion. The response of interface to the increase of p_w is similar to the previously reported confocal microscopy-based measurements [15,28] and conceptual description provided in Ref. [54]. At relatively low pressure, $1.0 < p_w < 1.3$ atm, θ_{CL} gradually increases to a maximum of $\theta_{adv} = 150^\circ$, while the contact line is pinned at the tip of groove, i.e., $h_{CL} = H$. Consistent with Refs. [19,20], the magnitude of θ_{adv} for the present hierarchical SHS is larger than the typical values of 110° – 120° observed for single-level topographies [14–18]. With increasing pressure to the $1.3 < p_w < 1.9$ atm range, the contact line depins from the tip of the groove while the interface shape remains nearly unchanged, with $\theta_{CL} \approx \theta_{adv}$. When p_w is subsequently reduced, the plastron recovers. However, the process is not symmetric, i.e., the interface does not recover to the same shape when p_w returns to the original level. Once p_w starts decreasing, θ_{CL} decreases immediately, unlike to compression phase, and h_{CL} increases gradually. Once p_w reaches 1.30 atm, the interface is nearly flat, i.e., $\theta_{CL} \sim 90^\circ$. Further reduction in p_w to the original pressure creates a convex interface, i.e., $\theta_{CL} < 90^\circ$. From the image at $t = 51$ min, it appears that the contact point of interface is located slightly below the tip of groove, presumably due to variations in the shape of the tip [Fig. 1(c)]. These findings are quantitatively consistent with the confocal microscopy results reported by Xue *et al.* [30] for a dimpled surface, including the asymmetry in contact angle for downward and upward migrations of interface. Using the measured plastron shape to estimate gas volume V_g and approximating p_g as p_w , i.e., neglecting surface tension and contribution of the water vapor, one can estimate the magnitude of $p_g V_g$ during the compression and decompression processes. Results (not presented) show that $p_g V_g$ deviates by a maximum of 5% from its initial magnitude, confirming that the gas in the plastron behaves like ideal gas for presumed isothermal conditions. The deviations might be caused by measurement uncertainty, surface tension effects, and limited mass diffusion.

The effect of mass diffusion out of the plastron caused by an increase in pressure, this time with flow, is summarized in Figs. 5(a)–5(d). Prior to each measurement series, p_w is set to a level above $p_v + p_\infty$, and then the water tunnel speed is increased and maintained at constant. For the samples shown, $p_w - (p_v + p_\infty) = 0.23$ atm and $\text{Re}_{\Theta 0} = 518$. At the initial state ($t = 0$), the plastron is still pinned to the tip of the groove. Since $J > 0$, the plastron slowly loses gas resulting in a decrease in h_{CL} and the interface height at the middle of the groove, h_m [defined in the sample image of Fig. 5(a)], as well as an increase in θ_{CL} . The evolution of interface shape is shown in Fig. 5(b), and quantitative results are presented in Figs. 5(c) and 5(d). The entire process could be separated into three stages. The first stage, which is denoted as “I,” occurs at $t < 60$ s. It is characterized by a pinned plastron, hence unchanged h_{CL} , as well as a gradually increasing θ_{CL} to $\theta_{adv} = 150^\circ$, and the corresponding slight decrease in h_m . During the second stage II, which takes place at $60 < t < 320$ s, the plastron is depinned, h_{CL} and h_m decrease at similar rates, and θ_{CL} remains nearly constant. At stage III, the interface touches the bottom of the groove, i.e., $h_m = 0$, and the two gas pockets remaining in the corners continue to shrink with h_{CL} decreasing at a slower rate. At $340 < t < 350$ s, the plastron is hard to quantify, and the shrinkage of h_{CL} appears to accelerate to nearly zero. The values of θ_{CL} during “III” are similar to stage “II.” At the present magnification, the pockets become invisible at $t = 350$ s. We cannot measure whether residual pockets remain with the nanotextures, but nanoplastrons are likely to persist given that the corresponding values of surface tension-induced pressure differences have magnitudes of several atmospheres.

Next, the flow in the tunnel is stopped, and the pressure is reduced to a level below $p_v + p_\infty$ and kept at constant for about 10 min. Although the water is supersaturated, there is no evidence of plastron growth at the present imaging resolution, presumably due to the slow diffusion rate in a stationary liquid. Then the velocity is increased back and maintained at $\text{Re}_{\Theta 0} = 518$, resulting in a slight decrease in test section pressure to $p_w - (p_v + p_\infty) = -0.07$ atm. The plastron recovery can also be divided to several stages. During stage I, the nucleation stage, small bubbles appear in a few

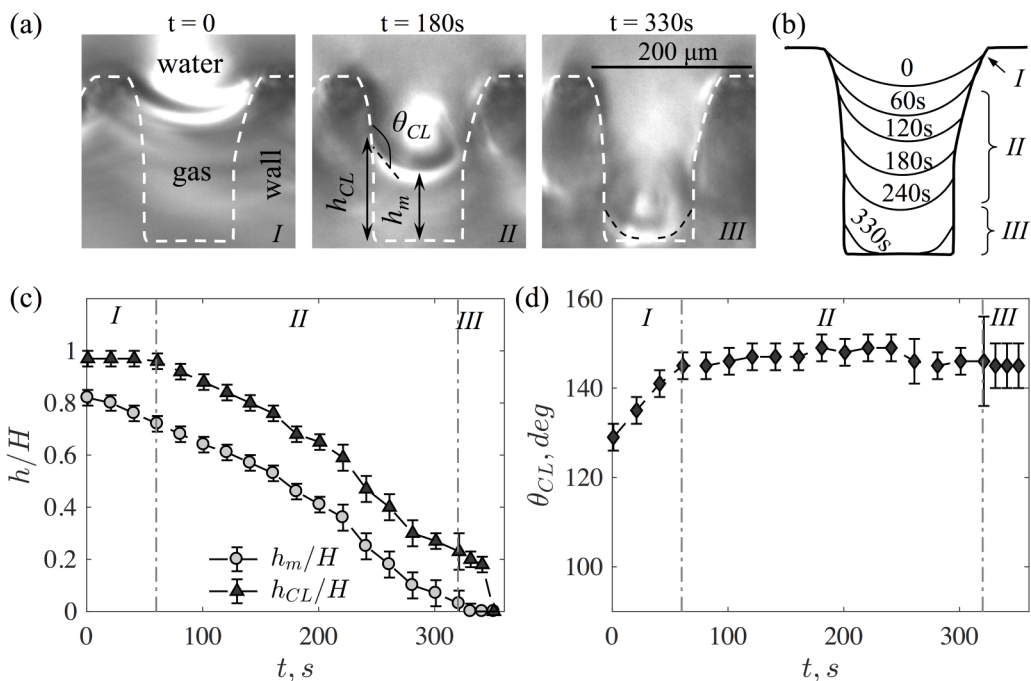


FIG. 5. A typical wetting transition due to gas diffusion from the plastron to liquid at a constant $p_w - p_v - p_\infty = 0.23$ atm and $\text{Re}_{\theta_0} = 518$: (a) selected images at the specified times; (b) measured schematics of the interface shape; (c) the average interface heights at the contact line and in the middle of the meniscus, as defined in image for $t = 180$ s; and (d) the average local contact angle.

seconds near the corner of the groove, as shown in Fig. 6(a). Figure 6(b) presents the evolution of the bubble radius for three sample cases, including the one corresponding to Fig. 6(a). Initially, the plastron grows radially from one of the two corners. The duration of this growth phase varies among different locations, falling in the 6–65 s range for the present samples. Once the bubble reaches the other corner, it flattens in a couple of seconds and then continues to grow while the interface

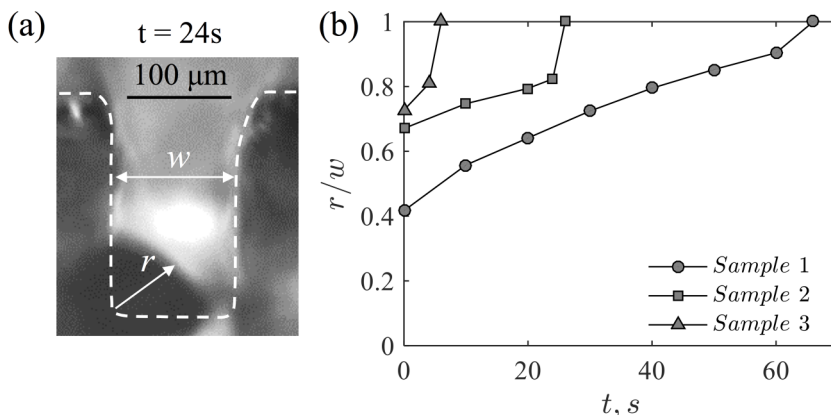


FIG. 6. Stage I corresponding to early phases of dewetting transition due to gas diffusion from the liquid to the plastron at $p_w - p_v - p_\infty = -0.07$ atm and $\text{Re}_{\theta_0} = 518$: (a) a sample image showing the bubble; (b) evolution of the bubble radius for three sample cases, with sample 2 corresponding to the image.

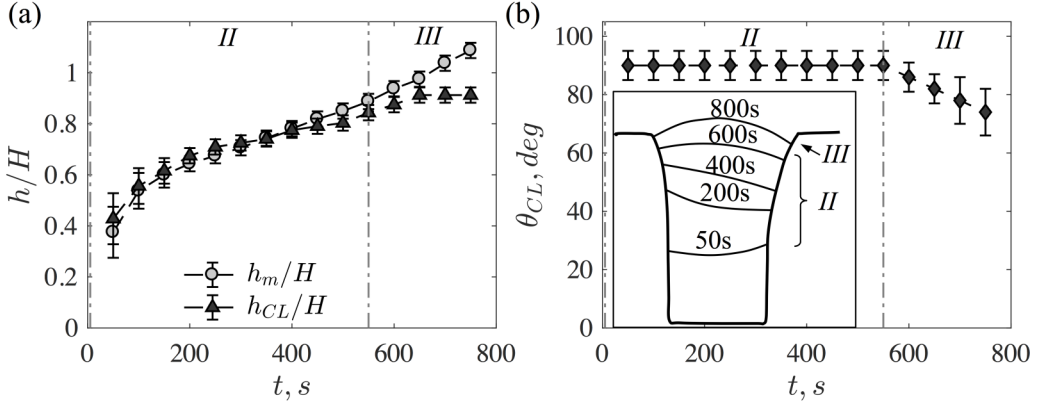


FIG. 7. Stages II and III of dewetting transition due to gas diffusion from liquid to plastron at $p_w - p_v - p_\infty = -0.07$ atm and $\text{Re}_{\Theta 0} = 518$: (a) the average interface heights at the contact line and in the middle of the meniscus; and (b) the average local contact angle, with the insert showing the interface shape.

remains large horizontal. The subsequent evolution of the plastron corresponding to sample 3 of Fig. 6(b) is summarized in Figs. 7(a) and 7(b). Included are plots of h_{CL} , h_m , θ_{CL} , and measured schematics of plastron shape. During stage II, the plastron reaches the so-called metastable stage [28], where it grows with $\theta_{CL} = 90^\circ$ and $h_{CL} \sim h_m$. The growth rate is faster initially ($t < 200$ s) and then becomes nearly constant at $200 < t < 600$ s. Subsequently, during stage III, the top of the plastron reaches at least one of the corners and becomes pinned to the tip of the grooves. Hence, a CB state is reached where the magnitudes of h_{CL} and h_m diverge, and θ_{CL} decreases as the interface becomes convex. The present trends during stage III, i.e., starting from a pinned contact line in a CB state, are qualitatively consistent with those observed before for dimpled surfaces in a laminar flow by Dilip *et al.* [24]. The nanobubbles that are likely to remain in the nanotextures may help in initializing the nucleation process, facilitating the plastron recovery process possible.

The above measurements of plastron change due to gas diffusion have been repeated for $p_w - (p_v + p_\infty)$ ranging from -0.07 to 0.23 atm, as well as four different $\text{Re}_{\Theta 0}$, as listed in Table I. The effect of p_w on the diffusion rate at the same $\text{Re}_{\Theta 0} = 518$ is summarized in Figs. 8(a)–8(e). Figure 8(a) shows the evolution of h_m . As expected, h_m decreases for $p_w > (p_v + p_\infty)$ and increases for $p_w < (p_v + p_\infty)$. The growth or decay rate increases with the magnitude of $p_w - (p_v + p_\infty)$. Figure 8(b) shows characteristic time scales, τ_{tr} , for wetting and dewetting transitions during stage II, i.e., when h_m is changing while θ_{CL} remains nearly constant. To ensure that the measurements are repeatable and that the interface can be clearly detected, τ_{tr} for wetting corresponds to h_m/H varying from 0.7 to 0.4, and the dewetting duration is based on h_m/H increasing from 0.6 to 0.9. These choices avoid the initial periods when the plastron changes its shape or the initial bubble growth period and reflect the same change in volume. The error bars in Fig. 8(b) reflect the uncertainty in plastron height measurements. As expected, τ_{tr} decreases with increasing magnitude of $p_w - (p_v + p_\infty)$, consistent with previous observations for stationary liquids [21–23,28]. Figure 8(c) shows the evolution of the same h_m/H , but now as a function of nondimensionalized time, $(t - t_0)/\tau_{tr}$, where t_0 is selected as the time when $h_m/H = 0.7$ and 0.6 for the wetting and dewetting processes, respectively. As is evident, the four wetting profiles collapse onto each other, and so do the two dewetting results.

Then, the magnitude of gas flux (J), can be estimated as $J = \rho_{\text{air}} \Delta h_m / \tau_{tr}$, where ρ_{air} is the density of air calculated from the pressure and temperature assuming ideal gas, and Δh_m is the change in interface height. The effects of evaporation and condensation of water on the plastron volume are neglected since the gas to vapor molar ratio is not expected to change as long as the temperature remains constant. In estimating the mass diffusion rate based on the interface height in the middle of the groove, one has to consider the potential impact of spanwise variation in

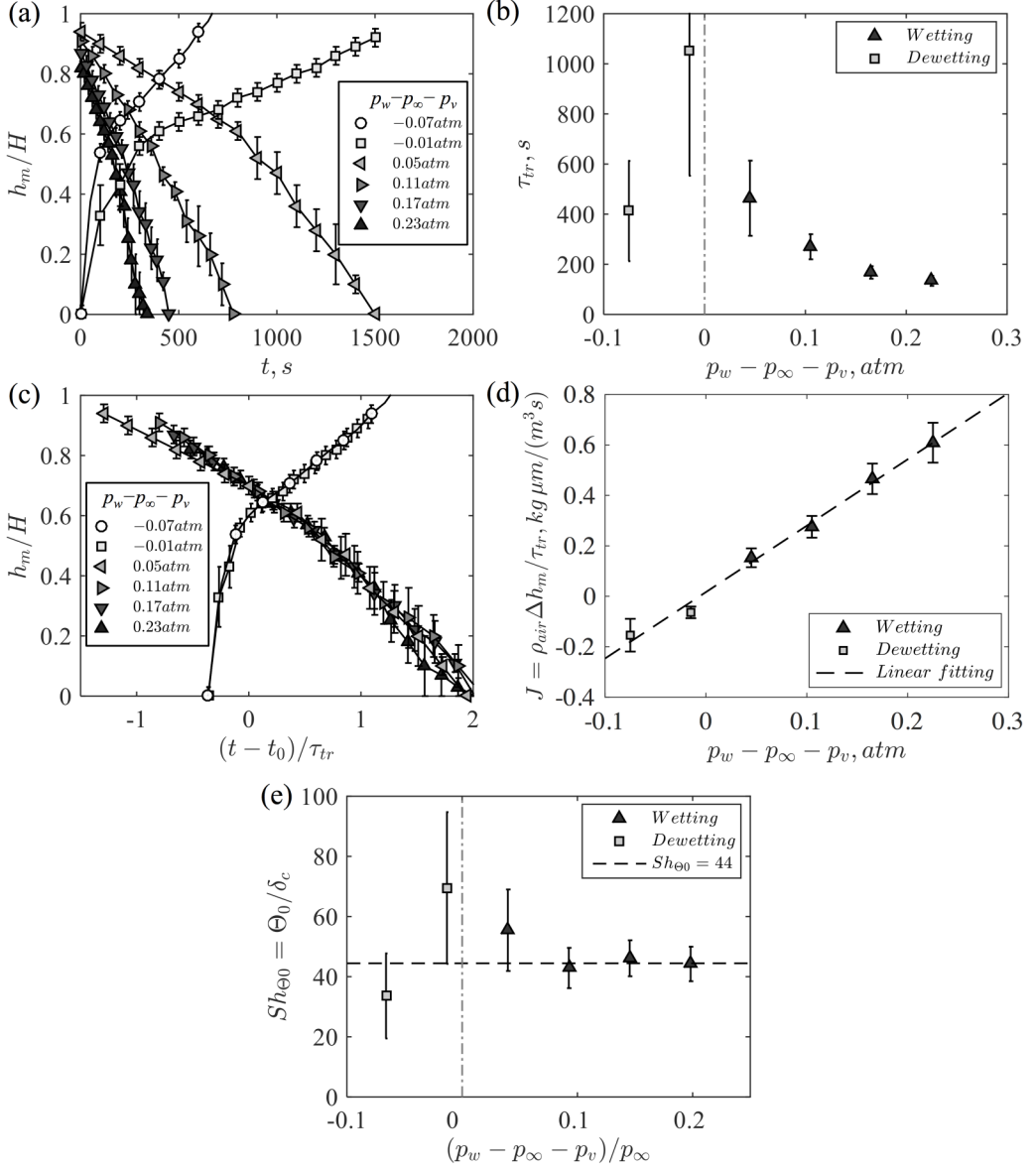


FIG. 8. Effect of pressure on the wetting and dewetting transitions at $Re_{\Theta_0} = 518$: (a) interface height for the specified pressures; (b) time scale for wetting and dewetting corresponding to h_m/H decreasing from 0.7 to 0.4, and dewetting based on h_m/H increasing from 0.6 to 0.9; (c) interface height replotted as a function of $(t - t_0)/\tau_{tr}$; (d) average rate of mass diffusion during τ_{tr} ; and (e) Sherwood number as a function of the dimensionless saturation pressure.

wall pressure and, consequently, plastron shape. According to Seo *et al.* [10], the wall pressure variation, Δp_w , for an SHS with a post geometry and a wavelength of 25 wall units, which is similar to the current highest Reynolds number case, is about $4\tau_w$. Therefore, under the present conditions, $\Delta p_w \sim 40$ Pa. Assuming a uniform p_p and $\theta_{CL} = 150^\circ$, the resulting variation in contact angle is $\Delta\theta_{CL} = w \Delta p_w / (2\gamma \sin\theta_{CL}) \sim 0.06$ rad, and the corresponding change to interface height is $\Delta h \sim w \Delta\theta_{CL} = 6 \mu m$. Hence, Δh is negligible compared to the length scale of the mass diffusion

process, and the changes to interface height at midspan can be used as a representative for calculating the magnitude of J . Figure 8(d) shows the calculated values of J for varying $p_w - (p_v + p_\infty)$, all for the same Reynolds number. As expected from Eq. (1), the present measurements confirm the linear relationship between J and $p_w - (p_v + p_\infty)$ for both wetting and dewetting transitions. The slope of this line, estimated by a least-square fit, can be used for calculating the diffusion length scale, $\delta_c = D(p_w - p_v - p_\infty)/(Jk_H)$. To normalize δ_c , we opt to use the momentum thickness of the smooth wall at the same freestream velocity (Θ_0) since the actual boundary layer thickness might change with interface height. As Table I indicates, there is a 5% difference between the momentum thicknesses corresponding to smooth and Wenzel state boundary layers for the same freestream velocity. This choice is discussed further later. The resulting Sherwood number is then

$$\text{Sh}_{\Theta_0} = \Theta_0/\delta_c = Jk_H\Theta_0/[D(p_w - p_v - p_\infty)]. \quad (2)$$

As is evident from Fig. 8(e), the magnitude of Sh_{Θ_0} does not change with pressure at $\text{Re}_{\Theta_0} = 518$ within the present uncertainty level.

The effect of Re_{Θ_0} on the rate of gas diffusion during wetting at a constant $p_w - (p_v + p_\infty) = 0.08$ atm is summarized in Figs. 9(a)–9(d). As is evident from Fig. 9(a), the wetting rate increases with increasing Re_{Θ_0} . Yet, Fig. 9(b) demonstrates that all the height profiles collapse when plotted as a function of $(t - t_0)/\tau_{tr}$. By calculating J and δ_c , following the procedures described above, Fig. 9(c)

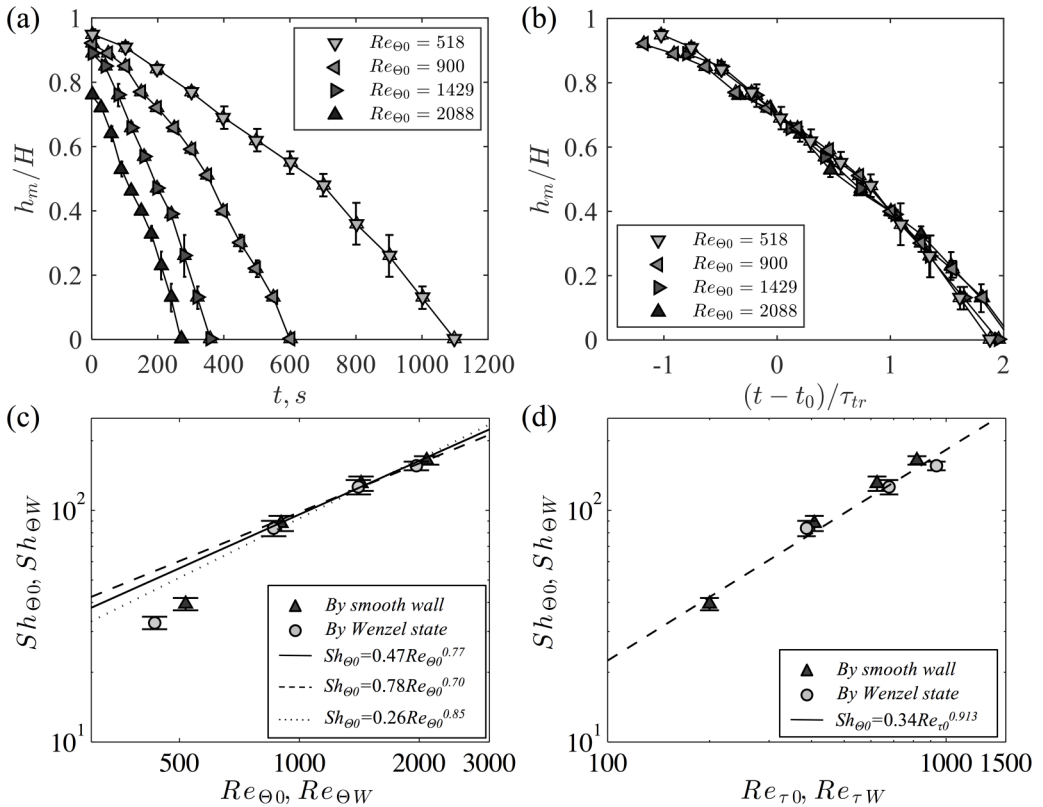


FIG. 9. Effect of Reynolds number on the wetting transition for $p_w - p_v - p_\infty = 0.08$ atm: (a) and (b) interface height; (c) relationships between Sherwood numbers and momentum thickness Reynolds numbers, with the solid line being a fit to the data point, and the dashed and dotted lines are bounding fits accounting for the uncertainty in the measurements; (d) relationships between Sherwood numbers and friction Reynolds numbers.

shows that the magnitude of $Sh_{\Theta 0}$ increases with increasing $Re_{\Theta 0}$. For $Re_{\Theta 0} > 800$, i.e., when the boundary layer is turbulent, the data suggest a power-law relationship, $Sh_{\Theta 0} = 0.47Re_{\Theta 0}^{0.77}$. This relationship is consistent with the typically observed trend for mass diffusion in a turbulent boundary layer over flat plate [38] and over SHSs [35], namely $Sh_x \propto Re_x^{0.8}$, which corresponds to $Sh_{\Theta 0} \propto Re_{\Theta 0}^{0.77}$, assuming that $\Theta_0/x \propto Re_x^{-0.1341}$ [47]. Here $Sh_x = x/\delta_c$, and $Re_x = U_0x/\nu$. According to [38], this power law is valid for a wide range of Schmidt numbers ($Sc = \nu/D$), namely, $0.5 \leq Sc \leq 1000$, including the current value of 500. It should be noted that the present analysis is performed for a limited range of Reynolds numbers. Due to the uncertainty in the data, Fig. 8(c) shows that the power law exponent falls in the 0.70–0.85 range. For $Re_{\Theta 0} = 518$, i.e., when the flat plate boundary layer is transitional, the magnitude of $Sh_{\Theta 0}$ is lower than that predicted by turbulent power law. This lower mass diffusion rate appears to correspond to a lower wall friction, as shown in Fig. 2(a). When the results are replotted as a function of $Re_{\tau 0}$, Fig. 9(d) shows that both transitional and turbulent flow regimes give the same power law $Sh_{\Theta 0} = 0.34Re_{\tau 0}^{0.913}$. This relationship can be predicted for the turbulent regime using $Sh_{\Theta 0} \propto Re_{\Theta 0}^{0.77}$ [Fig. 9(c)] and $Re_{\tau 0} \propto Re_{\Theta 0}^{0.843}$ [55]. The collapse of the transitional and turbulent flow data suggests that the Sherwood number is predominantly a function of the wall friction.

However, we should recall that the CB, Wenzel and smooth friction Reynolds numbers are different (Table I). The present flux measurements have been performed at the transition between CB to Wenzel states, when the groove is partially filled. For the present case where the wall friction has been measured directly in the CB state, corresponding to $Re_{\tau 0} = 820$ (Table I), the CB and smooth wall values of Re_{Θ} and Re_{τ} are close to each other. Hence, the same functional relationship is relevant when the groove is filled with air. Presenting the results using the Wenzel state momentum thicknesses, Fig. 9(c) confirms that the $Sh_{\Theta} = 0.47Re_{\Theta}^{0.77}$ relation is not affected since the Θ is included in both parameters. Conversely, relying on the log layer curve fit to estimate the Wenzel state $Re_{\tau W}$, notwithstanding the uncertainty involved, Fig. 9(d) shows that the power relation changes to $Sh_{\Theta W} \propto Re_{\tau W}^{0.70}$ for the turbulent cases.

IV. CONCLUSIONS

This experimental study investigates the effects of compression and gas diffusion on the volume of a plastron in a superhydrophobic surface for varying Reynolds numbers. For stationary water, the mass diffusion is slow. With increasing pressure, the wetting process involves initial pinning to the tip of the groove as the contact angle increases, followed by interface migration into the groove with an advancing contact angle of 150° . Upon subsequent decrease in pressure, the plastron growth involves brief pinning at the bottom edge of the groove, followed by upward interface migration, pinning at the tip corner, and formation of a convex interface.

With flow, the diffusion-induced wetting process observed during exposure to undersaturated liquid involves three phases: an initial pinned state, followed by downward migration at high contact angle, and shrinkage of bubbles at the bottom corners of the groove. At the end, the size of air pockets decreases below the present resolution limit. During this process, the boundary layer profile changes from slight drag reduction under the CB state to a rough wall boundary layer. Transition to supersaturated water by reducing the pressure initiates growth of a bubble from one of the bottom corners until it reaches the other side of the groove. Subsequently, the interface migrates upward at a low contact angle until it reaches the tips of the groove and then becomes convex. The diffusion rate increases with the magnitude of under- or supersaturation level and with increasing Reynolds number. A power law relation, $Sh_{\Theta 0} = 0.47Re_{\Theta 0}^{0.77}$, is obtained for the turbulent flow regime using the smooth wall momentum thickness for calculating the Sherwood ($Sh_{\Theta 0}$) and Reynolds ($Re_{\Theta 0}$) numbers. Conversely, mass diffusion in the transitional boundary layer is lower than this prediction. This power law agrees with diffusion rates observed previously for smooth wall turbulent boundary layers. However, when plotted against the friction Reynolds number ($Re_{\tau 0}$) instead, both the transitional and turbulent boundary layer results collapse onto a single power law, $Sh_{\Theta 0} = 0.34Re_{\tau 0}^{0.913}$. This trend suggests that turbulent diffusion and wall friction

are correlated. The relation between Sherwood number and momentum thickness Reynolds number persists if the Wenzel state length scales are used instead of those of the smooth wall. However, trends with the friction Reynolds number change slightly. These power laws provide quantitative guidance about the rate of plastron depletion with pressure, and could be used, e.g., for estimating the rate of replenishment required for maintaining a CB state. For future studies, it would be of interest to investigate the effect of the hierarchical structure of the SHS on the durability, i.e., its ability to recover after prolonged exposure to undersaturated water, as well as the mass diffusion rate from and into the plastron. The latter might be affected by the changes to the contact angle, plastron shape, and contact area associated with the nanotextures.

ACKNOWLEDGMENTS

This research has been performed under the ONR MURI program on Passive and Active Friction Drag Reduction of Turbulent Flows over Super-Hydrophobic Surfaces led by S. Ceccio. The program officer is K.-H. Kim. The authors also thank S. King and Y. Ronzhes for their assistance in setting up the experiments.

-
- [1] Y. Xue, P. Lv, H. Lin, and H. Duan, Underwater superhydrophobicity: Stability, design and regulation, and applications, *Appl. Mech. Rev.* **68**, 30803 (2016).
 - [2] J. P. Rothstein, Slip on superhydrophobic surfaces, *Annu. Rev. Fluid Mech.* **42**, 89 (2010).
 - [3] D. Saranadhi, D. Chen, J. A. Kleingartner, S. Srinivasan, R. E. Cohen, and G. H. McKinley, Sustained drag reduction in a turbulent flow using a low-temperature Leidenfrost surface, *Sci. Adv.* **2**, e1600686 (2016).
 - [4] M. Nosonovsky and B. Bhushan, Superhydrophobic surfaces and emerging applications: Non-adhesion, energy, green engineering, *Curr. Opin. Colloid Interface Sci.* **14**, 270 (2009).
 - [5] X. Zhang, F. Shi, J. Niu, Y. Jiang, and Z. Wang, Superhydrophobic surfaces: From structural control to functional application, *J. Mater. Chem.* **18**, 621 (2008).
 - [6] X.-M. Li, D. Reinhoudt, and M. Crego-Calama, What do we need for a superhydrophobic surface? A review on the recent progress in the preparation of superhydrophobic surfaces, *Chem. Soc. Rev.* **36**, 1350 (2007).
 - [7] C. Dorrer and J. Rühe, Some thoughts on superhydrophobic wetting, *Soft Matter* **5**, 51 (2009).
 - [8] D. Quéré, Wetting and roughness, *Annu. Rev. Mater. Res.* **38**, 71 (2008).
 - [9] E. Bormashenko, Progress in understanding wetting transitions on rough surfaces, *Adv. Colloid Interface Sci.* **222**, 92 (2014).
 - [10] J. Seo, R. García-Mayoral, and A. Mani, Pressure fluctuations and interfacial robustness in turbulent flows over superhydrophobic surfaces, *J. Fluid Mech.* **783**, 448 (2015).
 - [11] X. Tian, T. Verho, and R. H. A. Ras, Moving superhydrophobic surfaces toward real-world applications, *Science* **352**, 142 (2016).
 - [12] H. Ling, S. Srinivasan, K. Golovin, G. H. Mckinley, A. Tuteja, and J. Katz, High-resolution velocity measurement in the inner part of turbulent boundary layers over super-hydrophobic surfaces, *J. Fluid Mech.* **801**, 670 (2016).
 - [13] J. Bico, U. Thiele, and D. Quéré, Wetting of textured surfaces, *Colloids Surfaces A* **206**, 41 (2002).
 - [14] Q. S. Zheng, Y. Yu, and Z. H. Zhao, Effects of hydraulic pressure on the stability and transition of wetting modes of superhydrophobic surfaces, *Langmuir* **21**, 12207 (2005).
 - [15] P. Papadopoulos, L. Mammen, X. Deng, D. Vollmer, and H. Butt, How superhydrophobicity breaks down, *Proc. Natl. Acad. Sci. USA* **110**, 3254 (2013).
 - [16] H. M. Kwon, A. T. Paxson, K. K. Varanasi, and N. A. Patankar, Rapid Deceleration-Driven Wetting Transition During Pendant Drop Deposition on Superhydrophobic Surfaces, *Phys. Rev. Lett.* **106**, 036102 (2011).

- [17] C. W. Extrand, Repellency of the lotus leaf: Resistance to water intrusion under hydrostatic pressure, *Langmuir* **27**, 6920 (2011).
- [18] A. Checco, B. M. Ocko, A. Rahman, C. T. Black, M. Tasinkevych, A. Giacomello, and S. Dietrich, Collapse and Reversibility of the Superhydrophobic State on Nanotextured Surfaces, *Phys. Rev. Lett.* **112**, 216101 (2014).
- [19] Y. Xue, S. Chu, P. Lv, and H. Duan, Importance of hierarchical structures in wetting stability on submerged superhydrophobic surfaces, *Langmuir* **28**, 9440 (2012).
- [20] T. Verho, J. T. Korhonen, L. Sainiemi, V. Jokinen, C. Bower, K. Franze, S. Franssila, P. Andrew, O. Ikkala, and R. H. A. Ras, Reversible switching between superhydrophobic states on a hierarchically structured surface, *Proc. Natl. Acad. Sci. USA* **109**, 10210 (2012).
- [21] M. S. Bobji, S. V. Kumar, A. Asthana, and R. N. Govardhan, Underwater sustainability of the ‘Cassie’ state of wetting, *Langmuir* **25**, 12120 (2009).
- [22] R. Poetes, K. Holtzmann, K. Franze, and U. Steiner, Metastable Underwater Superhydrophobicity, *Phys. Rev. Lett.* **105**, 166104 (2010).
- [23] M. A. Samaha, H. Vahedi Tafreshi, and M. Gad-el-Hak, Sustainability of superhydrophobicity under pressure, *Phys. Fluids* **24**, 112103 (2012).
- [24] D. Dilip, N. K. Jha, R. N. Govardhan, and M. S. Bobji, Controlling air solubility to maintain ‘Cassie’ state for sustained drag reduction, *Colloids Surfaces A* **459**, 217 (2014).
- [25] D. Dilip, M. S. Bobji, and R. N. Govardhan, Effect of absolute pressure on flow through a textured hydrophobic microchannel, *Microfluid. Nanofluidics* **19**, 1409 (2015).
- [26] B. V. Hokmabad and S. Ghaemi, Effect of flow and particle-plastron collision on the longevity of superhydrophobicity, *Sci. Rep.* **7**, 41448 (2017).
- [27] M. A. Samaha, H. V. Tafreshi, and M. Gad-el-Hak, Influence of flow on longevity of superhydrophobic coatings, *Langmuir* **28**, 9759 (2012).
- [28] P. Lv, Y. Xue, Y. Shi, H. Lin, and H. Duan, Metastable States and Wetting Transition of Submerged Superhydrophobic Structures, *Phys. Rev. Lett.* **112**, 196101 (2014).
- [29] Y. Xiang, Y. Xue, P. Lv, D. Li, and H. Duan, Influence of fluid flow on the stability and wetting transition of submerged superhydrophobic surfaces, *Soft Matter* **12**, 4241 (2016).
- [30] Y. Xue, P. Lv, Y. Liu, Y. Shi, H. Lin, and H. Duan, Morphology of gas cavities on patterned hydrophobic surfaces under reduced pressure, *Phys. Fluids* **27**, 092003 (2015).
- [31] M. Xu, G. Sun, and C. J. Kim, Infinite Lifetime of Underwater Superhydrophobic States, *Phys. Rev. Lett.* **113**, 136103 (2014).
- [32] B. Emami, A. A. Hemeda, M. M. Amrei, A. Luzar, M. Gad-el-Hak, and H. Vahedi Tafreshi, Predicting longevity of submerged superhydrophobic surfaces with parallel grooves, *Phys. Fluids* **25**, 062108 (2013).
- [33] L. Piao and H. Park, Two-dimensional analysis of air-water interface on superhydrophobic grooves under fluctuating water pressure, *Langmuir* **31**, 8022 (2015).
- [34] C. Barth, M. Samaha, H. Tafreshi, and M. Gad-el-Hak, Convective mass transfer from submerged superhydrophobic surfaces, *Int. J. Flow Control* **5**, 79 (2013).
- [35] C. Barth, M. Samaha, H. Tafreshi, and M. Gad-el-Hak, Convective mass transfer from submerged superhydrophobic surfaces: Turbulent flow, *Int. J. Flow Control* **5**, 143 (2013).
- [36] E. L. Cussler, *Diffusion: Mass Transfer in Fluid Systems* (Cambridge University Press, Cambridge, 1997).
- [37] H. D. Baehr and K. Stephan, *Heat and Mass Transfer* (Springer, New York, 2006).
- [38] R. N. Sharma and S. U. Rahman, A simple model for turbulent boundary layer mass transfer on flat plate in parallel flow, *Chem. Eng. J.* **85**, 35 (2002).
- [39] S. Gopalan and J. Katz, Flow structure and modeling issues in the closure region of attached cavitation, *Phys. Fluids* **12**, 895 (2000).
- [40] X. Liu and J. Katz, Instantaneous pressure and material acceleration measurements using a four-exposure PIV system, *Exp. Fluids* **41**, 227 (2006).
- [41] P. Kim, M. J. Kreder, J. Alvarenga, and J. Aizenberg, Hierarchical or not? Effect of the length scale and hierarchy of the surface roughness on omniphobicity of lubricant-infused substrates, *Nano Lett.* **13**, 1793 (2013).

- [42] G. I. Roth and J. Katz, Five techniques for increasing the speed and accuracy of PIV interrogation, *Meas. Sci. Technol.* **12**, 238 (2001).
- [43] J. Sheng, E. Malkiel, and J. Katz, Using digital holographic microscopy for simultaneous measurements of 3D near wall velocity and wall shear stress in a turbulent boundary layer, *Exp. Fluids* **45**, 1023 (2008).
- [44] S. Talapatra and J. Katz, Three-dimensional velocity measurements in a roughness sublayer using microscopic digital in-line holography and optical index matching, *Meas. Sci. Technol.* **24**, 24004 (2013).
- [45] X. Wu and P. Moin, Transitional and turbulent boundary layer with heat transfer, *Phys. Fluids* **22**, 85105 (2010).
- [46] A. J. Smits, N. Matheson, and P. N. Joubert, Low-Reynolds-number turbulent boundary layers in zero and favorable pressure gradients, *J. Ship Res.* **27**, 147 (1983).
- [47] H. M. Nagib, K. A. Chauhan, and P. A. Monkewitz, Approach to an asymptotic state for zero pressure gradient turbulent boundary layers, *Philos. Trans. A* **365**, 755 (2007).
- [48] J. H. Lee, Turbulent boundary layer flow with a step change from smooth to rough surface, *Int. J. Heat Fluid Flow* **54**, 39 (2015).
- [49] R. F. Weiss, The solubility of nitrogen, oxygen and argon in water and seawater, *Deep Sea Res. Oceanog. Abs.* **17**, 721 (1970).
- [50] T. Min and J. Kim, Effects of hydrophobic surface on skin-friction drag, *Phys. Fluids* **16**, 55 (2004).
- [51] K. Fukagata, N. Kasagi, and P. Koumoutsakos, A theoretical prediction of friction drag reduction in turbulent flow by superhydrophobic surfaces, *Phys. Fluids* **18**, 051703 (2006).
- [52] J. Seo and A. Mani, On the scaling of the slip velocity in turbulent flows over superhydrophobic surfaces, *Phys. Fluids* **28**, 025110 (2016).
- [53] J. Jimenez, Turbulent flows over rough walls, *Annu. Rev. Fluid Mech.* **36**, 173 (2004).
- [54] D. Bartolo, F. Bouamrine, E. Verneuil, A. Buguin, P. Silberzan, and S. Moulinet, Bouncing or sticky droplets: Impalement transitions on superhydrophobic micropatterned surfaces, *Europhys. Lett.* **74**, 299 (2006).
- [55] P. Schlatter and R. Örlü, Assessment of direct numerical simulation data of turbulent boundary layers, *J. Fluid Mech.* **659**, 116 (2010).